ACS APPLIED MATERIALS & INTERFACES

www.acsami.org

Research Article

Integration of Graphene into Calcium Phosphate Coating for Implant Electronics

Elizaveta Dogadina, Raul D. Rodriguez,* Maxim Fatkullin, Anna Lipovka, Anna Kozelskaya, Andrey Averkiev, Evgenii Plotnikov, Xin Jia, Chaozong Liu, Jin-Ju Chen, Chong Cheng, Li Qiu, Sergei Tverdokhlebov, and Evgeniya Sheremet

Cite This: https://doi.org/10.1021/acsami.4c21046

Read Online

ACCESS | Metrics & More | Article Recommendations | Supporting Information

ABSTRACT: Bone injuries remain a significant challenge, driving the development of new materials and technologies to enhance healing. This study presents a novel approach for incorporating graphene into calcium phosphate (CaP) coatings on titanium alloy (Ti) substrates, with the aim of creating a new generation of materials for bone implant electronics. The stability of the composite coating under physiological conditions, long-term electrical and mechanical durability, and biocompatibility were systematically investigated. We integrated graphene into the CaP coating through the laser processing of diazonium-functionalized graphene films applied to the surface of CaP-coated Ti. The laser treatment induced several processes, including the removal of aryl groups, the formation of conductive pathways, and chemical bonding with the CaP film. As a result, the graphene−CaP nanocomposite demonstrated excellent mechanical durability, withstanding a 2 h sand abrasion test. It also exhibited excellent biocompatibility, as shown by the proliferation of human fibroblast cells for 7 days. The electrical properties remained stable under physiological conditions for 12 weeks, and the material maintained electrochemical stability after 1 million pulse cycles. Furthermore, it withstood the stress of 100,000 bending cycles without compromising electrical performance. This work highlights the versatility of the biocompatible graphene composite and its potential for a range of applications including free-form electronic circuits, electrodes, bending sensors, and electrothermal heaters.

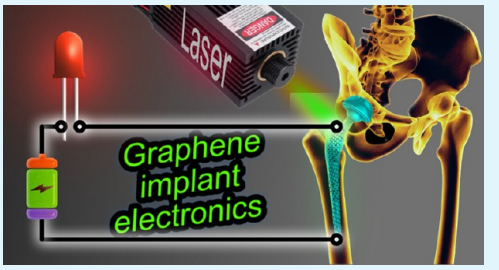

KEYWORDS: *graphene−calcium phosphate nanocomposites, laser processing, coatings, bone implants, biocompatible electronics*

1. INTRODUCTION

Advances in healthcare engineering have significantly improved human well-being, particularly through the use of implants to restore the lost functions of the musculoskeletal system. These innovations have reduced treatment times and patient rehabilitation, leading to a decrease in losses from socially significant diseases.[1,2] Progress in materials science and surface engineering has further enhanced the functionality and biocompatibility of orthopedic implants. To minimize rejection reactions (such as those seen in metallosis) and improve the survival rate of bone implants, their surfaces are commonly modified with CaP or hydroxyapatite coatings.[3,4] CaP is considered the gold standard for promoting bone regeneration[5] due to its excellent osteoinductivity, osteoconductivity, and similarity to bone composition.[6] The ability of CaP to release calcium and phosphate ions activates the growth and differentiation controlling signaling pathways, promotes bone mineral formation, and enhances the adsorption of extracellular matrix proteins and expression of osteoblastic differentiation markers.[7] Among surface modification techniques,[8−12] micro-arc oxidation (MAO) has gained significant attention for implant manufacturing due to its ability to produce high-hardness porous coatings[13] with strong adhesion and uniform coverage on complex geometries while remaining cost-effective and easy to implement.[13,14]

Graphene-based structures have emerged as a transformative addition to implant technology.[15] One promising approach is the integration of graphene and its derivatives into CaP coating or Ti.[16] These materials offer a range of advantageous properties,[17] including cell adhesion,[18] growth, osteogenesis,[19,20] biomineralization,[18] and mechanical resilience.[21] Several techniques, such as pulse electrodeposition,[22] plasma treatment,[12,23] and mixing,[24,25] have been employed to incorporate graphene into CaP coating. However, each of these methods has its limitations. For instance, plasma treatment and pulse electrodeposition are effective at creating surface strength and toughness but lack precise control over graphene distribution. In contrast, mixing techniques often

Received: November 30, 2024
Revised: February 4, 2025
Accepted: February 7, 2025

struggle to achieve a uniform graphene dispersion. These limitations hinder the full utilization of graphene's properties. Additionally, no study to date has investigated the application of graphene in implant electronics, where preserving and precisely controlling electrical properties are crucial. Applying various types of stimulations, such as mechanical,[26] magnetic,[27] electrical,[28] thermal/photothermal,[29] or releasing substances (e.g., growth factor),[30] are emerging strategies that can further enhance bone healing.[31] These advanced functionalities are expected to accelerate bone healing and improve patient outcomes. The incorporation of electrically conductive graphene into CaP surfaces offers the potential for developing smart implants[32] with integrated biocompatible electronics, offering promising advancements in orthopedic medicine.

To address this challenge, we aim to use laser processing to integrate graphene into a CaP-coated Ti substrate. Laser processing is gaining popularity due to its ability to precisely tune conductivity based on the specific requirements of electronic applications[33] and to create electronic structures with unique shapes and sizes,[34,35] opening applications such as sensors, energy storage, etc.[36−38] Here, we present a laser-based approach that offers benefits for implantable electronics. This method enables direct spatial control for fabricating biocompatible, conductive, and mechanically stable graphene patterns on implants, with minimal postprocessing compared to other techniques such as plasma treatment[11] or electrodeposition.[39] These advantages over traditional electronic manufacturing techniques include cost-effectiveness, scalability, the capability to produce mask-free arbitrary-shaped patterns, and compatibility with other methods, which promise to enhance functionality and improve production efficiency.[40,41]

This novel method for synthesizing graphene-based composites produces materials demonstrating mechanical and electrochemical stability under physiological conditions, overcoming graphene's biotoxicity issues and ensuring biocompatibility for biomedical applications. Cell viability tests confirm the composite's safety, which is essential for applications in implantable electronics for electrical and thermal stimulation and health monitoring. Laser-induced cross-linking strengthens the composite network, making it durable enough for long-term implantation in demanding environments. Furthermore, the composite demonstrates low impedance and electrochemical stability, minimizing the risk of device failure or degradation and making it suitable for a wide range of biomedical applications, including energy storage systems, actuators, and sensors.

2. MATERIALS AND METHODS

2.1. CaP Coating Fabrication by MAO. The Ti−6Al−4V alloy plates of size 20 × 20 × 0.5 mm^3 were used as substrates for coating fabrication. The formation of CaP coatings on the Ti plates was performed using the MAO setup "Microarc oxidation complex", which was designed in the Laboratory for Plasma Hybrid Systems at "The Weinberg Research Center", School of Nuclear Science & Engineering, Tomsk Polytechnic University. A supersaturated solution of CaO (reagent grade, Component-Reaktiv, LLC, Moscow, Russian Federation) in 10% H_3PO_4 (reagent grade, Component-Reaktiv, LLC, Moscow, Russian Federation) with 10 g/L of dispersed hydroxyapatite (reagent grade, Fluidinova, Maia, Portugal) was used as an electrolyte. The MAO process parameters were as follows: a voltage of 230 V, a voltage rise rate of 3 V/s, a pulse repetition frequency of 100 Hz, a pulse duration of 90 μs, and a formation time of 10 min.

2.2. LMod-G Coating Preparation. The technology of graphene modified with diazonium salts (Mod-G) powder synthesis was kept as published in our previous work.[42] Briefly, diazonium-functionalized graphene sheets were obtained by electrochemical exfoliation of a graphite electrode in the presence of 4-carboxybenzenediazonium tosylate. The potential difference between the Pt counter electrode and graphite electrode was 10 V. The concentration of diazonium salts was 0.032 g in 0.1 M H_2SO_4. The resulting powder was washed with water, ethanol, and acetone and then dried in air. Next, the powder was diluted in ethanol and sonicated to obtain a 4 mg/mL concentration dispersion.

The ethanolic dispersion of Mod-G was deposited on CaP/Ti by drop-coating at a volume of 25 μL cm^{-2}. Then, the film was left to dry under ambient conditions for 30 min. The thickness of the dried Mod-G films was about 15 μm.

A computer-controlled 436 nm laser diode was used to treat the Mod-G film on CaP/Ti. The optimal laser power of 1.6 W ensured the formation of a robust conductive composite structure, further denoted as LMod-G/CaP/Ti.

2.3. Raman Spectroscopy. Raman measurements were carried out using a confocal Raman microscope (NTEGRA Spectra, NT-MDT, Russia). The Raman microscope was configured with a 532 nm diode laser. The laser beam was focused on the LMod-G/CaP/Ti sample by using a 20× Mitutoyo objective with a 0.7 numerical aperture. The signal was collected by an electron-multiplying charge-coupled detector (EMCCD) (Andor Newton, U.K.) cooled down to −65 °C.

2.4. Atomic Force Microscopy (AFM) Examination. The surface morphology was investigated using an INTEGRA atomic force microscope (NT-MDT, Russia). The AFM images were obtained by scanning the sample surface with a conventional silicon cantilever. Dielectric force microscopy (DFM) and current-sensing atomic force microscopy (CSAFM) (KPFM) were performed using a Pt-coated tip in two-pass and single-pass modes, respectively.

2.5. X-ray Photoelectron Spectroscopy (XPS) Analysis. XPS was performed using a Thermo Fisher Scientific XPS NEXSA spectrometer with a monochromated Al Kα X-ray source working at 1486.6 eV. The survey scans were made with a pass energy of 200 eV and an energy resolution of 1 eV. For the high-resolution spectra, the pass energy was 50 eV, with an energy resolution of 0.1 eV. The analyzed area was 200 μm^2 in size. The flood gun was used for charge compensation.

2.6. Bending Tests. The three-point bending was controlled by a microprocessor and a step motor with continuous recording of the resistance changes during 100,000 cycles at a frequency of 1 Hz. The sample (60 × 3 mm^2) was bent 2 mm from the initial position at each cycle. The dependence of the voltage on the bending cycles was recorded using an Electrochemical Instruments P-45X potentiostat in the galvanostat mode.

2.7. Water Contact Angle Measurement. A 2 μL drop of deionized water was deposited on the sample surface and measured immediately using the system "DSA 100" (KRUSS, Germany). The contact angle was measured nine times at different locations on the sample surface to estimate the value of dispersion.

2.8. Electrothermal Heater. An electrothermal heater was operated by applying a voltage to the 20 mm^2 area via copper tape and silver paste contacts. A thermal image was recorded using a 60 × 60-pixel camera HT-02 from Hit (China) operating at a 40 cm distance from the sample when 2.5−10 V was applied.

2.9. Electrochemical Characterization. Electrochemical characterization was carried out in phosphate-buffered saline (PBS) using a three-electrode cell with LMod-G/CaP/Ti, platinum, and Ag/AgCl (saturated KCl) as the working, counter, and reference electrodes, respectively. Cyclic voltammetry (CV) measurements and electrochemical impedance spectroscopy (EIS) were carried out using a Corrtest CS2350 M instrument (Corrtest, China). EIS was measured in the frequency range of 1 Hz to 100 kHz.

2.10. 4-Point Probe Measurements. We used a potentiostat/galvanostat P-45X with an FRA-24 M impedance modulus (Electrochemical Instruments, Russia) in galvanostatic mode. An MST 4000A microprobe station (MS Tech Korea Co Ltd., South Korea) was used to position the tips in a square configuration with a 400 μm distance

https://doi.org/10.1021/acsami.4c21046
ACS Appl. Mater. Interfaces XXXX, XXX, XXX−XXX

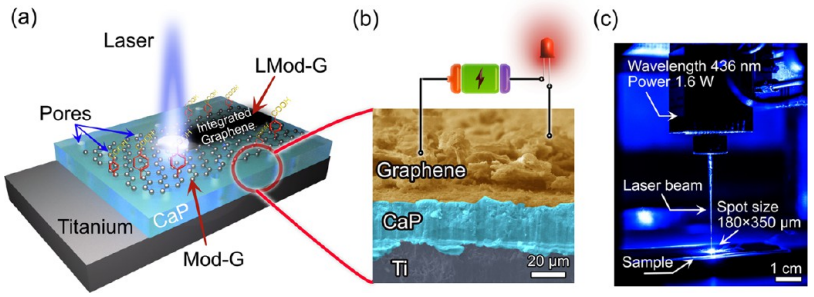

Figure 1. Concept sketch of the LMod-G/CaP/Ti fabrication. (a) Schematic illustration of laser-induced graphene integration in CaP coating on titanium alloy. (b) Cross-sectional SEM image of the interface between graphene layers and CaP, color-coded red and blue, respectively. (c) Picture of the laser processing setup.

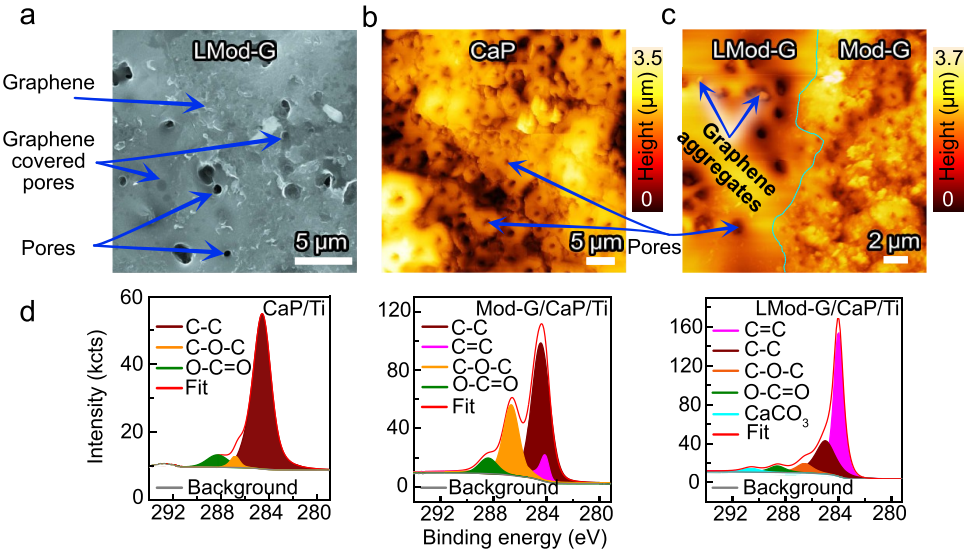

Figure 2. Microscopic, structural, and spectroscopic characterization. (a) Scanning electron microscopy microscopic, structural, and spectroscopic characterization. (a) SEM image of the laser-processed graphene layer on the top of the CaP/Ti surface. (b) AFM image of CaP. The pores in CaP are due to MAO deposition. (c) AFM image of the Mod-G/LMod-G interface. The dashed line is a guide for the eye for the interface between the two regions. (d) XPS C 1s narrow regions for the reference CaP/Ti substrate, Mod-G/CaP/Ti, and LMod-G/CaP/Ti samples. The samples used for AFM were washed in an ultrasonic bath before the experiments.

between each on the 1 × 1 cm^2 sample. The sheet resistance of the material was calculated using the following equation

$$R_{sheet} = \frac{R \times 2\pi}{\ln 2} \quad (1)$$

The resistance was measured four times at different locations on each sample to estimate the value of dispersion and statistics.

2.11. Cell Proliferation. Two samples were used to assess cell proliferation: CaP/Ti and LMod-G/CaP/Ti. All samples were immersed in 96% EtOH for 24 h to wash off possible organic contaminants and then sterilized in an autoclave at 121 °C for 20 min.

Human embryonic fibroblasts FECH-16-1 (Cell Culture Collection Laboratory, FBRI SRC VB "Vector", Rospotrebnadzor) and human osteosarcoma cell line HOS were cultured in DMEM culture media (Paneco LLC, Russia) supplemented with 2 mM glutamine (Paneco LLC, Russia), 10% FBS (Paneco LLC, Russia), and antibiotics penicillin/streptomycin mixture (Paneco LLC, Russia). Cells were grown in a CO_2 incubator (5% carbon dioxide) at 37 °C and 100% humidity. A standard MTT test was used for cell viability and proliferation measurement. The optical density of the samples was recorded at 570 nm on a Multiscan FC spectrophotometer (Thermo Fisher, MA). The data of optical densities obtained were processed, and the viability was calculated as a percentage of the control group to assess the level of proliferation or possible cytotoxic effects. To visually assess the morphology, proliferation, and cell growth on the sample surface, we used fluorescence microscopy with combined staining of Calcein AM (0.5 μg/mL) and Hoechst 33342 (1 μg/mL) and a set of appropriate light filters on a Zeiss Axio Vert.A1 microscope (Zeiss, Germany).

2.12. Finite Element Method (FEM) Modeling. The simulation of laser heating was performed using commercial software COMSOL Multiphysics, with the heat transfer in the solids module. Laser heating was modeled as a moving heat source on the sample surface. The sample contained four layers: Mod-G/CaP/TiO_2/Ti, from top to bottom, with thicknesses of 4/20/2/500 μm, respectively. In the CaP layer, 95 through holes with a radius of 1 μm were modeled in the laser pathway. The depth and width of the sample were set to 1.2 mm. The power was set to 1.6 W. The laser pulse time was set to 1.6 ms with a period of 2.6 ms. The radius of the laser spot was set to 74 μm. The time for the laser heating source to pass 1 mm was set to 240 ms. All parameters were chosen based on experimental measurements to represent the real conditions.

2.13. Scanning electron microscopy (SEM) and Elemental Mapping. SEM images were taken using a Quanta 200 3D system (FEI, Hillsboro, OR, USA) under high vacuum at U = 10 kV. Elemental mapping was conducted via energy-dispersive X-ray spectroscopy (EDX) using the same equipment.

2.14. X-ray diffraction (XRD) Analysis. XRD analysis was performed using an XRD-6000 diffractometer with CuKα radiation and a sliding beam. The operating voltage was maintained at 40 kV, with a current of up to 30 mA.

https://doi.org/10.1021/acsami.4c21046
ACS Appl. Mater. Interfaces XXXX, XXX, XXX−XXX

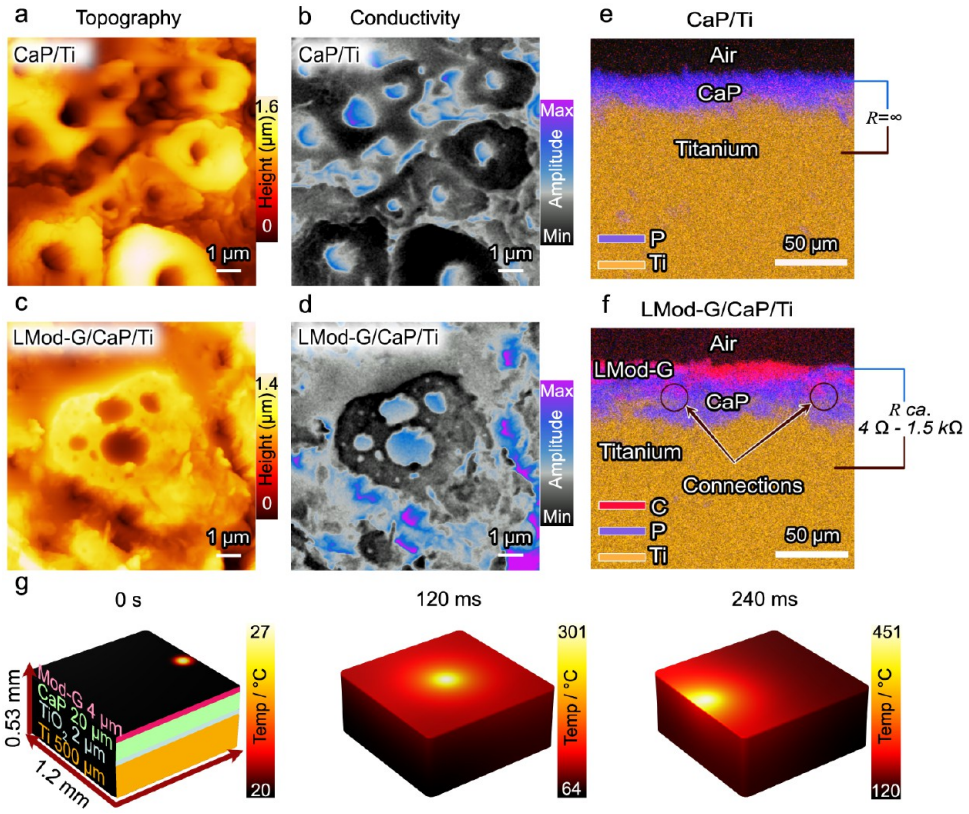

Figure 3. Structural, conductivity, and elemental imaging. (a, c) Surface topography by atomic force microscopy. (b, d) Sample conductivity imaging at the nanoscale by dielectric force microscopy. (e, f) Cross-sectional elemental mapping of the two samples, CaP/Ti and LMod-G/CaP/Ti. The different elements are shown overlaid with phosphor in blue, titanium in orange, and carbon in red. After laser processing, the electrical resistance values dramatically drop in the out-of-plane direction. In panel (f), Ti and C diffusion create electrically conductive paths (connections) that explain the resistance changes. (g) FEM simulation results at different times show the temperature distribution when the laser is scanned over the Mod-G/CaP/TiO_2/Ti sample.

3. RESULTS AND DISCUSSION

3.1. Formation and Spectroscopic Characterization.

We created an electrically conductive composite using laser processing of made from Mod-G films,[43] deposited on CaP-coated Ti plates (Figure 1a). Figure 1b presents a cross-sectional SEM image of the resulting layered structure (LMod-G, CaP, Ti). Mod-G, containing −COOH groups, forms a stable ethanolic suspension, enabling homogeneous film deposition on the CaP/Ti surface. In our previous work, AFM confirmed the nanoscale monolayer nature of Mod-G, with a single-layer thickness of 1.1 nm.[42] Here, we used a laser (Figure 1c) with a wavelength in the visible range (436 nm) to obtain an electrically conductive laser-modified graphene material. The main mechanism behind the conductivity restoration in Mod-G is the thermal homolysis of C−C bonds between graphene and functional groups. Conductivity is achieved by removing the aryl groups from the graphene sheets and transforming Csp^3 to Csp^2, restoring the conjugated carbon structure.[42] Laser parameters were optimized to achieve the highest mechanical robustness (assessed by the resistance to ultrasonic cleaning) and electrical conductivity of the composite (Table S1). This approach enables the direct fabrication of electrical circuits on CaP-coated Ti surfaces (bone implants) using laser processing technology.

The porous surface with microdefects in the CaP layer is typical for coatings obtained by MAO.[44,45] These microdefects result from plasma discharges, as described in detail by Jiang et al. and Kaseem et al.[13,46] Pores are clearly visible in the SEM and AFM images (Figure 2a−c). The Mod-G film morphology (Figure S1) differs significantly from the original CaP/Ti substrate, exhibiting a rough surface formed by randomly oriented Mod-G flakes. Laser processing notably affects the CaP surface microstructure. Pores in the CaP layer, covered by LMod-G, become more prominent and increase in size (Figure 2a), while the overall pore density decreases. This phenomenon is similar to Ostwald ripening[47,48] where smaller pores merge to reduce surface energy. These changes are attributed to the localized heating caused by laser annealing, which releases water vapor from the CaP layer, initiating grain growth and crystallization. To evaluate the adhesion of the graphene coating, we conducted AFM imaging analysis after ultrasonication of the LMod-G and Mod-G on the CaP/Ti substrate in ultrapure water. Figure 2c shows the interface morphology of LMod-G and Mod-G. After removing non-treated graphene residues, we observe the morphology of the original CaP surface (Figure 2b). The modifications in Mod-G caused by laser irradiation involve the photothermal removal of aryl groups under laser irradiation, which leads to the restoration of the graphene-like structure.[42,43]

Current sensing AFM results show that the transformation of Mod-G to conductive LMod-G on a CaP substrate is relatively homogeneous, as confirmed by a quite uniform electrical conductance of the LMod-G film (Figure S2). Control experiments involving laser treatment of bare CaP (without Mod-G) did not show changes in conductivity; the

https://doi.org/10.1021/acsami.4c21046
ACS Appl. Mater. Interfaces XXXX, XXX, XXX−XXX

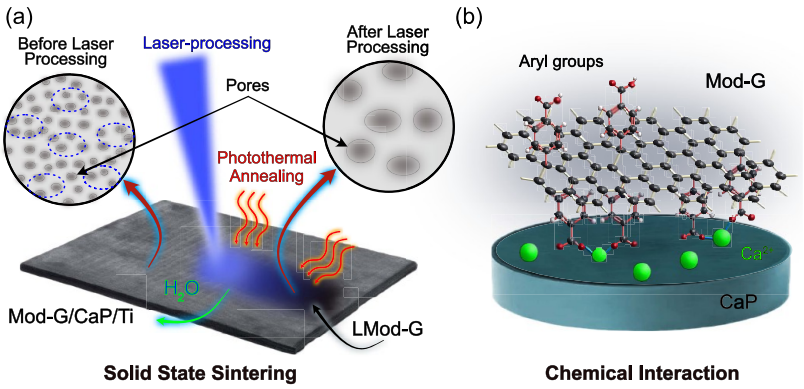

Figure 4. Composite formation mechanisms. (a) Laser-induced photothermal annealing and sintering. (b) Chemical interaction between the functional carboxylic groups in Mod-G and Ca^{2+} ions in the CaP layer.

surface remains electrically insulating regardless of the laser power used (see Figure S3).

The Raman spectra in Figure S4a show that the most prominent LMod-G peaks are the characteristic signatures of carbon materials: the defect-activated D band and the G band originating from sp^2 carbon.[49] The Raman spectral differences between LMod-G and Mod-G (Figure S5) reflect the structural changes due to laser processing and confirm the partial restoration of the sp^2-hybridized carbon network. The D/G intensity ratio (I_D/I_G) allows us to evaluate the areal defect density using the equation

$$n_d^2 = 7.3 \times 10^{-9} \cdot E_L^4\ [\mathrm{eV}^4] \frac{I_D}{I_G} \tag{2}$$

where E_L is the laser photon energy (λ = 532 nm → E_L = 2.33 eV).[50] After the laser processing, I_D/I_G drops from 1.3 ± 0.1 to 0.7 ± 0.1, reflecting a decrease in defect density from ca. (5.2 ± 0.2) × 10^{-4} to (3.9 ± 0.2) × 10^{-4} cm^{-2} (see Figure S5). These observations collectively support the partial restoration of the sp^2-hybridized carbon network and the reduction of structural defects upon laser processing.

The MAO process used to deposit the CaP layer results in the formation of titanium oxide,[44] as confirmed by the sharp peak at 144 cm^{-1} in the Raman spectra (Figure S4a). XPS provides surface element analysis for LMod-G/CaP/Ti (Figure S6). Notably, a decrease in the relative Ti content is accompanied by an increase in carbon due to Mod-G deposition, which screens the Ti substrate (Figures S4a and S5). Furthermore, a significant increase in the C═C bond (~284 eV) after laser processing (Figure 2d), together with a decrease in C−O−C and O−C═O bonds, confirms the successful laser-induced removal of aryl groups from Mod-G, which is in line with the previous studies.[42,43] Consistently with TiO_2 signal screening observed in Raman imaging results (Figure S4b), the deposited Mod-G film lacks phosphorus in the XPS O 1s region. However, after laser processing, PO_4 reveals again in the O 1s region, suggesting the formation of a laser-induced graphene−CaP mixture (Figure S7). Additional XPS spectra for the Ca 2p and P 2p regions are found in Figure S7. These observations with the AFM results obtained after ultrasonication indicate the formation of a composite structure that contributes to the robust adhesion of laser-processed graphene to the CaP-coated Ti implant surface.

3.2. Surface Microstructure and Electrical Conductivity. *3.2.1. Surface Conductivity.* Figure 3a,b illustrates the local electrical conductivity of the CaP/Ti composite as analyzed using DFM. Pores and cracks within CaP exhibit higher conductivity, attributed to the presence of Ti. This observation is based on the principle of DFM, where the tip oscillation amplitude correlates with charge carrier mobility and density.[51] The higher conductivity of pores and cracks is a direct consequence of MAO, resulting in deposits of Ti-rich domains along the pore walls. Similarly, in the laser-irradiated LMod-G/CaP/Ti sample (Figure 3c), cracks and pores exhibit the highest local electrical conductivity, as indicated by the purple coloration in Figure 3d. These conductive regions are attributed to the electrical conductivity of LMod-G, while CaP provide a conductive path for charge transfer between LMod-G and Ti. This observation is complemented by the conductive AFM results, and is discussed below.

3.2.2. Conductivity from LMod-G to Ti through CaP. To evaluate the electrical conductivity pathway between the Ti substrate and the LMod-G layer, we employed CSAFM. A potential difference was applied between the Ti plate and a metal-coated AFM tip, which was scanned over the LMod-G surface. The tip−sample current exhibited exceptionally high values for LMod-G. The inset in Figure S2d illustrates the conductivity of the sample characterized by rapid current saturation even at low potential values around 50 mV. This behavior significantly differs from that observed in Mod-G/Ca/Ti, where no current was detected between the tip and Ti substrate. Untreated Mod-G lacks in-plane conductivity due to the absence of delocalized electrons caused by the aryl functionalization.

Figure 3e,f presents electrical resistance data between the top layer of the sample and the Ti substrate. The electrical resistance of the sample changed significantly from infinity (CaP/Ti) to about 1.5 kΩ (LMod-G/CaP/Ti) after laser processing. EDX results suggest that LMod-G and Ti establish electrical connections via the CaP layer, as illustrated in Figure 3f. Cross-sectional Raman data in Figure S8 support this, confirming graphene's presence in the CaP layer of LMod-G/CaP/Ti.

An interesting observation is presented on the right side of Figure 3f. The resistance between the top LMod-G layer and the Ti substrate could be switched from kΩ to a few Ω by applying voltage above 10 V (see Notes S1−S3 for details). This suggests that the composite exhibits two potential current pathways: in-plane (Table S2 and Figure S9) and out-of-plane, as discussed in more detail in Note S4.

3.2.3. Mechanism for Laser-Driven Graphene Integration into CaP Composite. The formation of the graphene−CaP

https://doi.org/10.1021/acsami.4c21046
ACS Appl. Mater. Interfaces XXXX, XXX, XXX−XXX

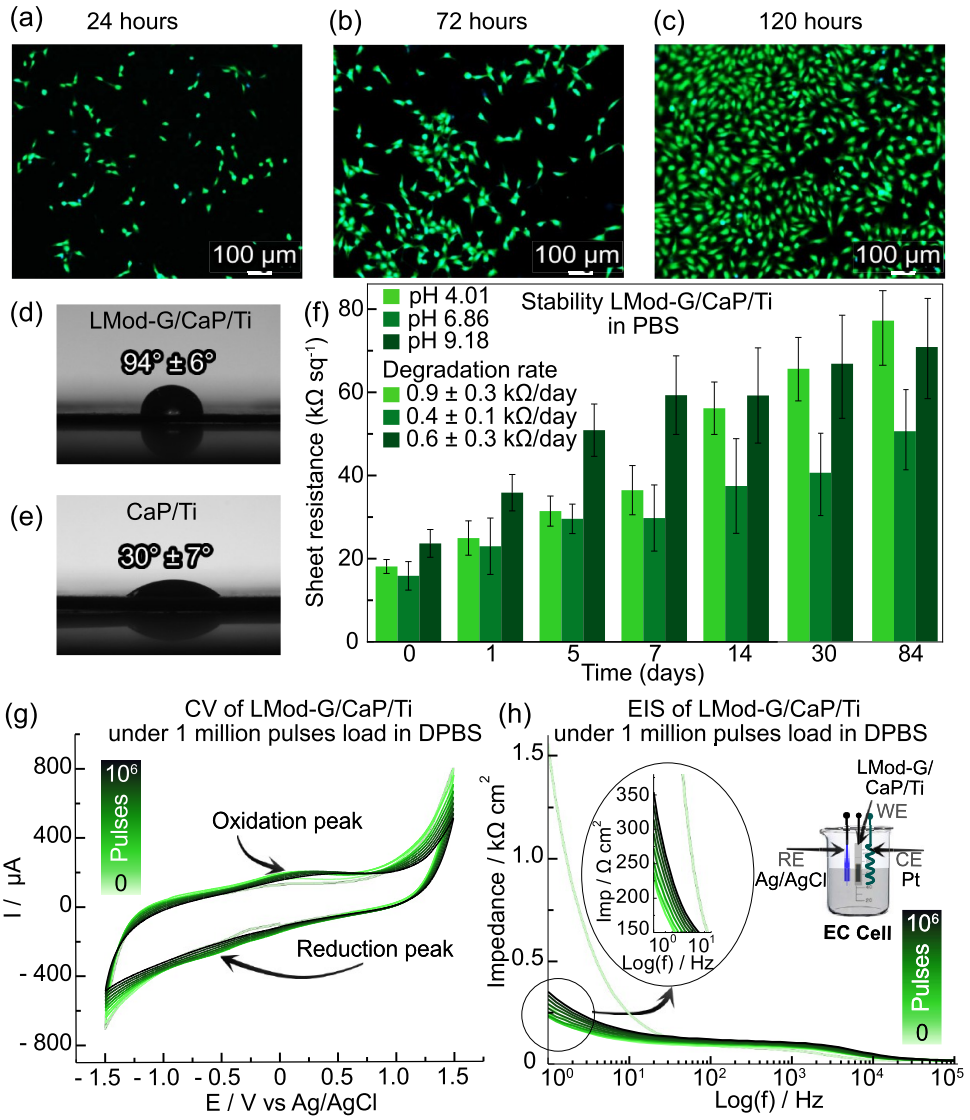

Figure 5. Cell viability, surface hydrophilicity, and electrochemical analyses. (a–c) Optical images of human osteosarcoma HOS cells grown on an LMod-G/CaP composite for 24, 72, and 120 h, respectively. (d, e) Contact angle values for CaP coating and LMod-G/CaP composite. (f) Stability of LMod-G/CaP/Ti composite in PBS solution with different pH values under 37 °C. (g) CV of LMod-G/CaP/Ti under multipulse load. (h) EIS of LMod-G/CaP/Ti under multipulse load.

composite is closely related to two factors: laser-induced heating and chemical interactions between Mod-G and CaP.

Accurately measuring the temperatures reached during laser irradiation at small spatial scales is challenging, therefore, we used FEM simulations to estimate the contribution of photothermal heating. The FEM modeling results in Figure 3g suggest that temperatures as high as 451 °C could be achieved during laser scanning across the sample. This value is a conservative lower limit because such factors as surface roughness, pores, and optical absorption changes (which are not accounted for in the model) can lead to higher temperatures.[52] Laser processing leads to changes in the pores of LMod-G/CaP as was evidenced with AFM. Specifically, the pores enlarge but become less densely distributed (Figure 2c). These morphological changes result from the photothermal heating enabled by the Mod-G film, which acts as a photothermal transducer. This photothermal effect is similar to observations made with other nanomaterials on polymer substrates.[53]

The composite formation begins with solid-state laser sintering[54] between LMod-G and CaP. During this process, laser-induced pore enlargement allows for greater accumulation of graphene, thereby enhancing its integration and establishing an electrically conductive graphene–CaP network on the Ti substrate (Figure 4a).

XRD (Figure S10) confirmed the amorphous nature of the original CaP layer.[55] Phase transitions in CaP occur in the range of 500–1200 °C, converting amorphous CaP to crystalline phases (e.g., α-tricalcium phosphate, anhydrous dicalcium phosphate, and octacalcium phosphate) as reported previously.[56,57] Raman spectroscopy (Figure S4) verified laser-induced crystallization, with a PO_4 group peak shift from 950 to 960 cm^{-1}, indicating thermal-induced crystallization.[58]

Figure S11 illustrates the differences in Raman spectra between the non-laser-treated region and the LMod-G/CaP/Ti sample. A broad Raman peak, ranging from 924 to 1146 cm^{-1}, is observed in the non-treated region, suggesting the presence of amorphous CaP. In contrast, the LMod-G/CaP/Ti

https://doi.org/10.1021/acsami.4c21046
ACS Appl. Mater. Interfaces XXXX, XXX, XXX–XXX

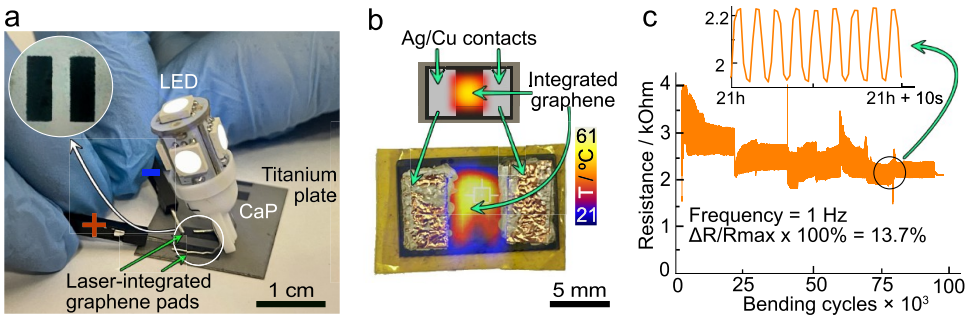

Figure 6. Proof-of-concept graphene-Ti implant electronics. (a) Picture of a superbright LED being powered through the graphene composite conductors made on the CaP/Ti surface. (b) An image of an electrothermal heater with the sketch is shown at the bottom. (c) The electrical resistance of an LMod-G/CaP/Ti sample as a function of bending cycles. The inset evidences periodic changes in resistance within some cycles with a resistance variation of 13.7%.

sample exhibits three distinct peaks at 945, 980, and 1075 cm^{-1}, indicating the formation of crystalline phases.[56]

Both photothermal effects and chemical interactions contribute to the integration of Mod-G (and LMod-G) with CaP. The strong affinity between the functional carboxylic groups in Mod-G and Ca^{2+} ions in the CaP layer[59,60] results in strong adhesion between the two materials (Figure 4b). This chemical aspect, combined with the photothermal effects induced by laser irradiation, contributes to the adhesion process, ensuring composite stability suitable for a wide range of practical applications.

3.3. Mechanical and Physiological Stability, Biocompatibility, and Proof-of-Concept Applications. It is crucial to assess the cytotoxicity of the resulting composite to evaluate the potential for utilizing conductive graphene-based patterns on CaP and Ti in various biomedical applications. In this regard, we conducted cell viability studies involving human fibroblast and human osteosarcoma HOS cell cultures over 7 days, following the guidelines outlined in the ISO 10993−5 standard for the biological evaluation of medical devices.

Figure 5a−c presents the fluorescence images of HOS cells after 24, 72, and 120 h with cell densities 91 ± 12.9, 211 ± 27.0, and 631 ± 153.2 cells/mm^2, respectively. A conventional polystyrene Petri dish was used as a comparative control to evaluate cell growth on the CaP/Ti and LMod-G/CaP/Ti substrates. The fluorescence microscopy results (Figure S12a−f) clearly illustrate excellent biocompatibility. Moreover, the cell viability comparison presented in Figure S12g,h shows that the integration of graphene via laser processing did not compromise the inherent biocompatibility of CaP. This is exciting since the aryl group removal turns the surface more graphene-like, and, therefore, more hydrophobic, with the presence of sharp edges, which could affect cell membrane integrity.[61] This composite formation strategy effectively mitigated graphene toxicity. In addition to the biocompatibility, we examined the electrical properties after cell culturing. The sheet resistance has not changed much (from 1267.2 ± 60.7 to 1213.7 ± 276.5 Ω/sq) after cell culture application, with an increase in uncertainties (60.7 and 276.5 Ω/sq), indicating an impact on resistance variability across the sample. The change in wetting properties was demonstrated by the 3-fold increase in contact angles from CaP to LMod-G/CaP/Ti observed in Figure 5d,e. Hydrophilic surfaces are conventionally considered more suitable for cell cultures due to their better cell and protein adhesion properties. On the other hand, a hydrophobic surface without negative consequences for cells should offer advantages for implantation to the possible suppression of biofouling.

To assess biofouling, we tested the effect of different solutions (PBS, DMEM, and DMEM with proteins) on electron-transfer processes by recording CVs with $K_3[Fe(CN)_6]$ (Figure S13). Two redox peaks appeared: an anodic peak at 0.5 V and a cathodic peak at −0.2 V for PBS and DMEM, shifting to 1.0 and −0.3 V in DMEM with proteins. After 10 cycles, the current dropped notably in DMEM and DMEM with proteins, indicating that the hydrophobic surface does not prevent protein and organic adsorption. These results could be interpreted in two ways. While protein adsorption promotes cell integration to the implant surface,[62] biofouling could hinder signal delivery in implantable electronics. For a comprehensive understanding, *in vivo* assessment is required.

To further evaluate the potential of LMod-G/CaP/Ti as an implant material, we performed tests to assess its mechanical, electrochemical, and electrical stabilities under physiological conditions. We immersed samples in PBS with different pH values (4.01, 6.86, and 9.18) under 37 °C, and monitored the sheet resistance during various immersion periods (1, 5, 7, 14, 30, and 84 days). Despite variations in resistance during the testing period, it consistently remained within the acceptable range for electronic applications (electrical/thermal stimulation),[63] as illustrated in Figure 5f. Notably, the electrical conductivity persisted for 12 weeks, corresponding to the average bone healing time, and demonstrating long-term stability.[64]

To evaluate its potential as a cell electrical stimulation device, we tested the electrochemical stability under 1 million bipolar pulses (1.5 V, 3 ms, 100 Hz), following parameters from the literature.[65,66] Changes in the properties were monitored every 100,000 pulses using CV (Figure 5g) and EIS (Figure 5h) in Dulbecco's phosphate-buffered saline (DPBS). A minor reduction peak at −0.5 V gradually decreases, disappearing after 700,000 pulses, suggesting the removal of residual LMod-G functional groups. Furthermore, an oxidation peak at 0.1 V shifts to 0.3 V, with each 100,000 pulse likely due to the oxidation of LMod-G, Ti, or both.

EIS results indicate a slight decrease at low frequencies, possibly due to the processes discussed. The most significant changes (~80% for 1 Hz) occur after the first 100,000 pulses, with the impedance deviation stabilizing to about 20%, suggesting electrochemical stability. Therefore, electrochemical post-treatment is recommended. All the material has high sheet resistance, its low impedance makes the material suitable for

https://doi.org/10.1021/acsami.4c21046
ACS Appl. Mater. Interfaces XXXX, XXX, XXX−XXX

effective signal transmission at relevant frequencies for biomedical implants.

To assess mechanical stability, we carried out a 3 h abrasion test, rotating the sample in sand at 1.3 Hz without encapsulation. The sheet resistance was measured before and after 1, 2, and 3 h. Initially, the sheet resistance was 1.3 ± 0.1 kΩ sq^{-1} and remained stable at 1.2 ± 0.6 kΩ sq^{-1} after 1 h, with slight dispersion. However, after 2 h, the sheet resistance spiked to 130 ± 100 kΩ sq^{-1}, and by the 3rd hour, conductivity was entirely lost (∞ Ω sq^{-1}).

The Raman maps in Figure S14 show the intensity of the G band coming from LMod-G after 3 h of abrasion. These results indicate that graphene layers remain on the surface, although below the percolation threshold required for surface conductivity. The material performance in a 1 h abrasion test indicates its potential durability and longevity in practical applications. This test simulates extreme conditions beyond those typically encountered in the body, indicating promising resilience and capability for sustained operation, thus highlighting its suitability for long-term applications.

The properties of LMod-G/CaP/Ti, including electrical and mechanical stabilities, encouraged us to explore its potential in electronic device applications. To demonstrate the feasibility of creating free-form electric circuits, we used laser processing to fabricate conductive tracks on the Mod-G, CaP, and Ti composites, as shown in Figure 6a. These laser-patterned tracks served as contact pads to power an LED stack, illustrating the potential of our approach for designing and creating customized implant electronics.

Furthermore, we designed an electrical heater using the LMod-G/CaP/Ti composite, as shown in Figure 6b, with temperature measurements captured by a thermal camera. This outcome has implications for integrating thermal therapy[67] and sterilization functions into an implant (Figure S15). This application goes in line with previous works using laser-induced graphene/PDMS Joule heaters,[68] although in our case, this is the first time laser processing has been used for such an application on an implant surface.

In addition, Figure 6c demonstrates the nanocomposite's mechanical stability under continuous deformation, highlighting its potential as a bending sensor. Throughout testing, only minor resistance changes were observed with peak-to-peak variations above the noise level, as shown in the inset.

This study investigated the composite morphology and element content, formation process, and properties. While *in vivo* investigations are beyond the scope of this work, they are a critical next step. Future research will include more complex biological settings, such as *in vivo* studies, to assess the material degradation, biocompatibility, and osteogenic properties,[16] as well as changes in electrical conductivity and mechanical stability after implantation.

These results provide a glimpse of the potential of graphene−titanium implant electronics. We also explored TiO_2 coatings (Table S3), which yielded similarly robust patterns. Furthermore, free-form patterning allows us to design elements like antennas and chemiresistor sensors, as was recently shown with polymer and textile substrates.[43,69]

4. CONCLUSIONS

This study demonstrates, for the first time, the successful fabrication of biocompatible, electrically conductive, mechanically, and electrochemically stable graphene/CaP/Ti composites using a laser-based approach. The laser-induced integration into CaP helps overcome graphene's biotoxicity concerns, unlocking the creation of safe and functional implantable devices. The mechanism behind this composite involves precise laser energy applied to functionalized graphene films on CaP, which induces interfacial bonding between the composite layers and CaP recrystallization.

We also evidenced a strong adhesion between functionalized graphene and CaP due to chemical interactions contributing to the composite stability. This laser-based direct-writing method allows the scalable and cost-effective fabrication of functional graphene-based features directly on implants. It combines adaptability to complex implant shapes, precision, mask-free spatial control, and compatibility with current laser manufacturing as well as with other electronic manufacturing methods, which are promising for enhancing functionality and improving production efficiency.

The demonstrated applications, including bending circuit prototypes, durable biocompatible electrodes, and electrothermal heaters, align with emerging paradigms such as the Internet of Bodies and Medical Things, highlighting the potential for transforming medical technology and healthcare. While further research, including *in vivo* studies and clinical trials, as well as detailed cost and yield analysis, is necessary to fully translate this research into industrial settings, this work provides a strong foundation for graphene integration into future implantable devices where biocompatibility and functionality are critical.

■ ASSOCIATED CONTENT

Supporting Information

The Supporting Information is available free of charge at https://pubs.acs.org/doi/10.1021/acsami.4c21046.

SEM image of Mod-G film on the top of the CaP/Ti surface (Figure S1); CSAFM results for Mod-G and LMod-G (Figure S2); the conductivity measurements of CaP and Mod-G before and after laser processing (Figure S3); Raman spectra of the CaP, Mod-G, and LMod-G regions (Figure S4); Raman spectra of LMod-G/CaP/Ti and Mod-G/CaP/Ti (Figure S5); XPS survey spectra for the elemental composition of the CaP/Ti substrate, Mod-G/CaP/Ti, and LMod-G/CaP/Ti samples (Figure S6); XPS O 1s, Ca 2p, P 2p, and Ti 2p narrow regions for the CaP/Ti substrate, Mod-G/CaP/Ti, and LMod-G/CaP/Ti samples (Figure S7); Raman cross-sectional analysis for the LMod-G sample (Figure S8); the resistance measurements depend on the distance between the contact, with a graph showing linear resistance vs distance (Figure S9); XRD of CaP/Ti, LCaP/Ti, Mod-G/CaP/Ti, and LMod-G/CaP/Ti (Figure S10); Raman spectra were recorded from Mod-G/CaP/Ti and LMod-G/CaP/T (Figure S11); optical images of human osteosarcoma HOS cells grown on a Petri dish, CaP coating, and LMod-G/CaP composites (Figure S12); CVs from LMod-G/CaP/Ti electrodes measured with 100 mV/s scan rates (Figure S13); graphene's G mode Raman intensity maps after 1, 2, and 3 h of abrasion show the persistence of graphene (Figure S14); picture of an electrothermal heater with the sketch shown at the bottom after applying a high voltage (Figure S15); selection of optimal laser parameters (Table S1); the resistance value depends on the distance between the contact (Table S2); and selection of

https://doi.org/10.1021/acsami.4c21046
ACS Appl. Mater. Interfaces XXXX, XXX, XXX−XXX

optimal laser parameters for TiO_2 coating (Table S3); discussion on shortcutting LMod-G and Ti (Note S1); control experiment on an LMod-G/CaP/Ti sample at high voltage (Note S2); control experiment on a CaP/Ti sample at high voltage (Note S3); summary of the conductive properties of the composite (Note S4) (PDF)

AUTHOR INFORMATION

Corresponding Author

Raul D. Rodriguez − *Tomsk Polytechnic University, Tomsk 634050, Russia;* orcid.org/0000-0003-4016-1469; Email: raul@tpu.ru

Authors

Elizaveta Dogadina − *Tomsk Polytechnic University, Tomsk 634050, Russia*

Maxim Fatkullin − *Tomsk Polytechnic University, Tomsk 634050, Russia*

Anna Lipovka − *Tomsk Polytechnic University, Tomsk 634050, Russia;* orcid.org/0000-0002-2012-1569

Anna Kozelskaya − *Tomsk Polytechnic University, Tomsk 634050, Russia*

Andrey Averkiev − *Tomsk Polytechnic University, Tomsk 634050, Russia*

Evgenii Plotnikov − *Tomsk Polytechnic University, Tomsk 634050, Russia*

Xin Jia − *School of Chemistry and Chemical Engineering, State Key Laboratory Incubation Base for Green Processing of Chemical Engineering, Shihezi University, Shihezi 832003 Xinjiang, China;* orcid.org/0000-0002-4114-8680

Chaozong Liu − *Institute of Orthopaedic & Musculoskeletal Science, Royal National Orthopaedic Hospital, University College London, Stanmore HA7 4LP, U.K.*

Jin-Ju Chen − *The School of Materials and Energy, University of Electronic Science and Technology of China, Chengdu 610054, China;* orcid.org/0000-0002-3455-6838

Chong Cheng − *College of Polymer Science and Engineering, State Key Laboratory of Polymer Materials Engineering, Sichuan University, Chengdu 610065, China;* orcid.org/0000-0002-6872-2240

Li Qiu − *College of Polymer Science and Engineering, State Key Laboratory of Polymer Materials Engineering, Sichuan University, Chengdu 610065, China;* orcid.org/0000-0003-2685-9799

Sergei Tverdokhlebov − *Tomsk Polytechnic University, Tomsk 634050, Russia;* orcid.org/0000-0002-2242-6358

Evgeniya Sheremet − *Tomsk Polytechnic University, Tomsk 634050, Russia;* orcid.org/0000-0003-3937-8628

Complete contact information is available at: https://pubs.acs.org/10.1021/acsami.4c21046

Notes

The authors declare no competing financial interest.

ACKNOWLEDGMENTS

The authors thank the support from TPU Priority 2030-NIP/IZ-007-0000-2022. The fabrication of CaP coatings was funded by the Ministry of Science and Higher Education of the Russian Federation, Project Nauka FSWW-2023-0007. C.L. would like to thank the support of the Royal Society via an International Exchange program (Grant No. IEC \R2\202134). C.C. and L.Q. acknowledge the funding of the National Natural Science Foundation of China (Nos. 52161145402, 52173133) and the Sichuan Science and Technology Program (No. 2023YFH0008). The authors acknowledge the Agrochemical Engineering Innovation and Intelligence Base for Oasis Ecology. J.-J.C. thanks the support from the Chengdu Science and Technology Program (Grant No. 2023-GH02-00021-HZ). The authors thank the Central Laboratories of TPU (Analytical Center) for the XPS measurements, and Alina Gorbunova for operating the equipment. Work was conducted using equipment from the Tomsk Regional Core Shared Research Facilities Centre of National Research Tomsk State University.

REFERENCES

(1) Lewis, S. R.; Macey, R.; Eardley, W. G.; Dixon, J. R.; Cook, J.; Griffin, X. L. Internal Fixation Implants for Intracapsular Hip Fractures in Older Adults. *Cochrane Database Syst. Rev.* **2021**, *3* (3), No. CD013409.

(2) Kim, T.; See, C. W.; Li, X.; Zhu, D. Orthopedic Implants and Devices for Bone Fractures and Defects: Past, Present and Perspective. *Eng. Regener.* **2020**, *1*, 6−18.

(3) Bohara, S.; Suthakorn, J. Surface Coating of Orthopedic Implant to Enhance the Osseointegration and Reduction of Bacterial Colonization: A Review. *Biomater. Res.* **2022**, *26* (1), 26.

(4) Lu, X.; Wu, Z.; Xu, K.; Wang, X.; Wang, S.; Qiu, H.; Li, X.; Chen, J. Multifunctional Coatings of Titanium Implants Toward Promoting Osseointegration and Preventing Infection: Recent Developments. *Front. Bioeng. Biotechnol.* **2021**, *9*, No. 783816.

(5) Tavoni, M.; Dapporto, M.; Tampieri, A.; Sprio, S. Bioactive Calcium Phosphate-Based Composites for Bone Regeneration. *J. Compos. Sci.* **2021**, *5* (9), 227.

(6) Xiao, D.; Zhang, J.; Zhang, C.; Barbieri, D.; Yuan, H.; Moroni, L.; Feng, G. The Role of Calcium Phosphate Surface Structure in Osteogenesis and the Mechanisms Involved. *Acta Biomater.* **2020**, *106*, 22−33.

(7) Jeong, J.; Kim, J. H.; Shim, J. H.; Hwang, N. S.; Heo, C. Y. Bioactive Calcium Phosphate Materials and Applications in Bone Regeneration. *Biomater. Res.* **2019**, *23*, 4.

(8) Gu, Y. W.; Khor, K. A.; Cheang, P. In Vitro Studies of Plasma-Sprayed hydroxyapatite/Ti-6Al-4V Composite Coatings in Simulated Body Fluid (SBF). *Biomaterials* **2003**, *24* (9), 1603−1611.

(9) Minagar, S.; Berndt, C. C.; Wang, J.; Ivanova, E.; Wen, C. A Review of the Application of Anodization for the Fabrication of Nanotubes on Metal Implant Surfaces. *Acta Biomater.* **2012**, *8* (8), 2875−2888.

(10) Jelinek, M. Hybrid Laser Technology for Biomaterials. In *Lasers for Medical Applications*; Elsevier, 2013; pp 704−724.

(11) Chiang, W.-H.; Mariotti, D.; Sankaran, R. M.; Eden, J. G.; Ostrikov, K. K. Microplasmas for Advanced Materials and Devices. *Adv. Mater.* **2020**, *32* (18), No. 1905508.

(12) Wong, P.-C.; Kurniawan, D.; Wu, J.-L.; Wang, W.-R.; Chen, K.-H.; Chen, C.-Y.; Chen, Y.-C.; Veeramuthu, L.; Kuo, C.-C.; Ostrikov, K. K.; Chiang, W.-H. Plasma-Enabled Graphene Quantum Dot Hydrogel-Magnesium Composites as Bioactive Scaffolds for In Vivo Bone Defect Repair. *ACS Appl. Mater. Interfaces* **2023**, *15* (38), 44607−44620.

(13) Kaseem, M.; Fatimah, S.; Nashrah, N.; Ko, Y. G. Recent Progress in Surface Modification of Metals Coated by Plasma Electrolytic Oxidation: Principle, Structure, and Performance. *Prog. Mater. Sci.* **2021**, *117*, No. 100735.

(14) Aliofkhazraei, M.; Macdonald, D. D.; Matykina, E.; Parfenov, E. V.; Egorkin, V. S.; Curran, J. A.; Troughton, S. C.; Sinebryukhov, S. L.; Gnedenkov, S. V.; Lampke, T.; Simchen, F.; Nabavi, H. F. Review of Plasma Electrolytic Oxidation of Titanium Substrates: Mechanism, Properties, Applications and Limitations. *Appl. Surf. Sci. Adv.* **2021**, *5*, No. 100121.

(15) Harun, S. W. *Handbook of Graphene, Volume 7: Biomaterials*; John Wiley & Sons, 2019.
(16) Shin, Y. C.; Bae, J.-H.; Lee, J. H.; Raja, I. S.; Kang, M. S.; Kim, B.; Hong, S. W.; Huh, J.-B.; Han, D.-W. Enhanced Osseointegration of Dental Implants with Reduced Graphene Oxide Coating. *Biomater. Res.* **2022**, *26* (1), 11.
(17) Kang, M. S.; Jeong, S. J.; Lee, S. H.; Kim, B.; Hong, S. W.; Lee, J. H.; Han, D.-W. Reduced Graphene Oxide Coating Enhances Osteogenic Differentiation of Human Mesenchymal Stem Cells on Ti Surfaces. *Biomater. Res.* **2021**, *25* (1), 4.
(18) Daneshmandi, L.; Barajaa, M.; Tahmasbi Rad, A.; Sydlik, S. A.; Laurencin, C. T. Graphene-Based Biomaterials for Bone Regenerative Engineering: A Comprehensive Review of the Field and Considerations Regarding Biocompatibility and Biodegradation. *Adv. Healthcare Mater.* **2021**, *10* (1), No. 2001414.
(19) Daneshmandi, L.; Holt, B. D.; Arnold, A. M.; Laurencin, C. T.; Sydlik, S. A. Ultra-Low Binder Content 3D Printed Calcium Phosphate Graphene Scaffolds as Resorbable, Osteoinductive Matrices That Support Bone Formation in Vivo. *Sci. Rep.* **2022**, *12* (1), No. 6960.
(20) Farshid, S.; et al. Electrophoretic Deposition of Biphasic Calcium Phosphate/graphene Nanocomposite Coatings on Ti6Al4V Substrate for Biomedical Applications. *J. Alloys Compd.* **2022**, *892*, No. 162150.
(21) Seonwoo, H.; Choung, H.-W.; Park, S.; Choi, K. S.; Jang, K.-J.; Kim, J.; Lim, K.-T.; Kim, Y.; Garg, P.; Pandey, S.; Lee, J.; Park, J.-C.; Choung, Y.-H.; Choung, P.-H.; Kim, S. Y.; Chung, J. H. Reduced Graphene Oxide-Incorporated Calcium Phosphate Cements with Pulsed Electromagnetic Fields for Bone Regeneration. *RSC Adv.* **2022**, *12* (9), 5557−5570.
(22) Fathyunes, L.; Khalil-Allafi, J.; Moosavifar, M. Development of Graphene Oxide/calcium Phosphate Coating by Pulse Electrodeposition on Anodized Titanium: Biocorrosion and Mechanical Behavior. *J. Mech. Behav. Biomed. Mater.* **2019**, *90*, 575−586.
(23) Khan, P. A.; Thoutam, A. K.; Gopal, V.; Gurumallesh, A.; Joshi, S.; Palaniappan, A.; Markocsan, N.; Manivasagam, G. Influence of Graphene Nanoplatelets on the Performance of Axial Suspension Plasma-Sprayed Hydroxyapatite Coatings. *Bioengineering* **2023**, *10* (1), No. 44.
(24) Lee, J. H.; Shin, Y. C.; Lee, S.-M.; Jin, O. S.; Kang, S. H.; Hong, S. W.; Jeong, C.-M.; Huh, J. B.; Han, D.-W. Enhanced Osteogenesis by Reduced Graphene Oxide/Hydroxyapatite Nanocomposites. *Sci. Rep.* **2015**, *5*, No. 18833.
(25) Kim, J.-W.; Shin, Y. C.; Lee, J.-J.; Bae, E.-B.; Jeon, Y.-C.; Jeong, C.-M.; Yun, M.-J.; Lee, S.-H.; Han, D.-W.; Huh, J.-B. The Effect of Reduced Graphene Oxide-Coated Biphasic Calcium Phosphate Bone Graft Material on Osteogenesis. *Int. J. Mol. Sci.* **2017**, *18* (8), No. 1725.
(26) Ouyang, N.; Zhang, P.; Fu, R.; Shen, G.; Jiang, L.; Fang, B. Mechanical Strain Promotes Osteogenic Differentiation of Bone Mesenchymal Stem Cells from Ovariectomized Rats via the Phosphoinositide 3-kinase/Akt Signaling Pathway. *Mol. Med. Rep.* **2018**, *17* (1), 1855−1862.
(27) Yan, F.; Liu, Z.; Zhang, T.; Zhang, Q.; Chen, Y.; Xie, Y.; Lei, J.; Cai, L. Biphasic Injectable Bone Cement with FeO/GO Nanocomposites for the Minimally Invasive Treatment of Tumor-Induced Bone Destruction. *ACS Biomater Sci. Eng.* **2019**, *5* (11), 5833−5843.
(28) Ferrigno, B.; Bordett, R.; Duraisamy, N.; Moskow, J.; Arul, M. R.; Rudraiah, S.; Nukavarapu, S. P.; Vella, A. T.; Kumbar, S. G. Bioactive Polymeric Materials and Electrical Stimulation Strategies for Musculoskeletal Tissue Repair and Regeneration. *Bioact. Mater.* **2020**, *5* (3), 468−485.
(29) Zhang, X.; Cheng, G.; Xing, X.; Liu, J.; Cheng, Y.; Ye, T.; Wang, Q.; Xiao, X.; Li, Z.; Deng, H. Near-Infrared Light-Triggered Porous AuPd Alloy Nanoparticles To Produce Mild Localized Heat To Accelerate Bone Regeneration. *J. Phys. Chem. Lett.* **2019**, *10* (15), 4185−4191.
(30) Habraken, W. J. E. M.; Boerman, O. C.; Wolke, J. G. C.; Mikos, A. G.; Jansen, J. A. In Vitro Growth Factor Release from Injectable Calcium Phosphate Cements Containing Gelatin Microspheres. *J. Biomed. Mater. Res., Part A* **2009**, *91A* (2), 614−622.
(31) Zhang, X.; Wang, T.; Zhang, Z.; Liu, H.; Li, L.; Wang, A.; Ouyang, J.; Xie, T.; Zhang, L.; Xue, J.; Tao, W. Electrical Stimulation System Based on Electroactive Biomaterials for Bone Tissue Engineering. *Mater. Today* **2023**, *68*, 177−203.
(32) Abyzova, E.; Dogadina, E.; Rodriguez, R. D.; Petrov, I.; Kolesnikova, Y.; Zhou, M.; Liu, C.; Sheremet, E. Beyond Tissue Replacement: The Emerging Role of Smart Implants in Healthcare. *Mater. Today Bio* **2023**, *22*, No. 100784.
(33) Rodriguez, R. D.; Fatkullin, M.; Garcia, A.; Petrov, I.; Averkiev, A.; Lipovka, A.; Lu, L.; Shchadenko, S.; Wang, R.; Sun, J.; Li, Q.; Jia, X.; Cheng, C.; Kanoun, O.; Sheremet, E. Laser-Engineered Multifunctional Graphene-Glass Electronics. *Adv. Mater.* **2022**, *34* (43), No. 2206877.
(34) You, R.; Liu, Y.-Q.; Hao, Y.-L.; Han, D.-D.; Zhang, Y.-L.; You, Z. Laser Fabrication of Graphene-Based Flexible Electronics. *Adv. Mater.* **2020**, *32* (15), No. 1901981.
(35) Wan, Z.; Streed, E. W.; Lobino, M.; Wang, S.; Sang, R. T.; Cole, I. S.; Thiel, D. V.; Li, Q. Laser-reduced Graphene: Synthesis, Properties, and Applications. *Adv. Mater. Technol.* **2018**, *3* (4), No. 1700315.
(36) Fatkullin, M.; Dogadina, E.; Bril', I. 'ya; Ivanov, A.; Matkovic, A.; Rodriguez, R. D.; Sheremet, E.; Rodriguez, R. D. Nanomaterials/polymer-Integrated Flexible Sensors: A Full-Laser-Processing Approach for Real-Time Analyte Monitoring. *IEEE Sens. J.* **2024**, *24* (9), 13816−13822.
(37) Lipovka, A.; Garcia, A.; Abyzova, E.; Fatkullin, M.; Song, Z.; Li, Y.; Wang, R.; Rodriguez, R. D.; Sheremet, E. Laser Processing of Emerging Nanomaterials for Optoelectronics and Photocatalysis. *Adv. Opt. Mater.* **2024**, *12* (17), No. 2303194.
(38) Kogolev, D.; Kurtsevich, E.; Fatkullin, M.; Zinovyev, A.; Gorbunova, A.; Rodriguez, R. D.; Guselnikova, O.; Boukherroub, R.; Postnikov, P. S. Laser-Induced Carbonization of Ni-BDC Layer on PET: Functional Upcycling of Polymer Wastes towards Bend Resistive Sensor. *Mater. Today Commun.* **2024**, *39*, No. 108843.
(39) Nizami, M. Z. I.; Campéon, B. D. L.; Nishina, Y. Electrodeposition of Hydroxyapatite and Graphene Oxide Improves the Bioactivity of Medical Grade Stainless Steel. *Materials Today Sustainability* **2022**, *19*, No. 100193.
(40) Ko, S. H.; Pan, H.; Grigoropoulos, C. P.; Luscombe, C. K.; Fréchet, J. M. J.; Poulikakos, D. All-Inkjet-Printed Flexible Electronics Fabrication on a Polymer Substrate by Low-Temperature High-Resolution Selective Laser Sintering of Metal Nanoparticles. *Nanotechnology* **2007**, *18* (34), No. 345202.
(41) Kapnopoulos, C.; Zachariadis, A.; Mekeridis, E.; Kassavetis, S.; Gravalidis, C.; Laskarakis, A.; Logothetidis, S. On-the-Fly Short-Pulse R2R Laser Patterning Processes for the Manufacturing of Fully Printed Semitransparent Organic Photovoltaics. *Materials* **2022**, *15* (22), No. 8218.
(42) Rodriguez, R. D.; Khalelov, A.; Postnikov, P. S.; Lipovka, A.; Dorozhko, E.; Amin, I.; Murastov, G. V.; Chen, J.-J.; Sheng, W.; Trusova, M. E.; Chehimi, M. M.; Sheremet, E. Beyond Graphene Oxide: Laser Engineering Functionalized Graphene for Flexible Electronics. *Mater. Horiz.* **2020**, *7* (4), 1030−1041.
(43) Lipovka, A.; Petrov, I.; Fatkullin, M.; Murastov, G.; Ivanov, A.; Villa, N. E.; Shchadenko, S.; Averkiev, A.; Chernova, A.; Gubarev, F.; Saqib, M.; Sheng, W.; Chen, J.-J.; Kanoun, O.; Amin, I.; Rodriguez, R. D.; Sheremet, E. Photoinduced Flexible Graphene/polymer Nanocomposites: Design, Formation Mechanism, and Properties Engineering. *Carbon* **2022**, *194*, 154−161.
(44) Wang, Y.; Yu, H.; Chen, C.; Zhao, Z. Review of the Biocompatibility of Micro-Arc Oxidation Coated Titanium Alloys. *Mater. Des.* **2015**, *85*, 640−652.
(45) Kozelskaya, A. I.; Rutkowski, S.; Frueh, J.; Gogolev, A. S.; Chistyakov, S. G.; Gnedenkov, S. V.; Sinebryukhov, S. L.; Frueh, A.; Egorkin, V. S.; Choynzonov, E. L.; Buldakov, M.; Kulbakin, D. E.; Bolbasov, E. N.; Gryaznov, A. P.; Verzunova, K. N.; Apostolova, M. D.; Tverdokhlebov, S. I. Surface Modification of Additively Fabricated

https://doi.org/10.1021/acsami.4c21046
ACS Appl. Mater. Interfaces XXXX, XXX, XXX−XXX

Titanium-Based Implants by Means of Bioactive Micro-Arc Oxidation Coatings for Bone Replacement. *J. Funct. Biomater.* **2022**, *13* (4), No. 285.
(46) Jiang, B. L.; Wang, Y. M. Plasma Electrolytic Oxidation Treatment of Aluminium and Titanium Alloys. In *Surface Engineering of Light Alloys*; Elsevier, 2010; pp 110−154.
(47) Liu, Y.; Shen, Z. Dehydroxylation of Hydroxyapatite in Dense Bulk Ceramics Sintered by Spark Plasma Sintering. *J. Eur. Ceram. Soc.* **2012**, *32* (11), 2691−2696.
(48) Gross, K. A.; Gross, V.; Berndt, C. C. Thermal Analysis of Amorphous Phases in Hydroxyapatite Coatings. *J. Am. Ceram. Soc.* **1998**, *81* (1), 106−112.
(49) Malard, L. M.; Pimenta, M. A.; Dresselhaus, G.; Dresselhaus, M. S. Raman Spectroscopy in Graphene. *Phys. Rep.* **2009**, *473* (5−6), 51−87.
(50) Ferrari, A. C.; Basko, D. M. Raman Spectroscopy as a Versatile Tool for Studying the Properties of Graphene. *Nat. Nanotechnol.* **2013**, *8* (4), 235−246.
(51) Zhang, J.; Lu, W.; Li, Y. S.; Cai, J.; Chen, L. Dielectric Force Microscopy: Imaging Charge Carriers in Nanomaterials without Electrical Contacts. *Acc. Chem. Res.* **2015**, *48* (7), 1788−1796.
(52) Lu, Y.-W.; Li, L.-Y.; Liu, J.-F. Influence of Surface Roughness on Strong Light-Matter Interaction of a Quantum Emitter-Metallic Nanoparticle System. *Sci. Rep.* **2018**, *8* (1), No. 7115.
(53) Rodriguez, R. D.; Shchadenko, S.; Murastov, G.; Lipovka, A.; Fatkullin, M.; Petrov, I.; Tran, T.-H.; Khalelov, A.; Saqib, M.; Villa, N. E.; Bogoslovskiy, V.; Wang, Y.; Hu, C.-G.; Zinovyev, A.; Sheng, W.; Chen, J.-J.; Amin, I.; Sheremet, E. Ultra-robust Flexible Electronics by Laser-driven Polymer-nanomaterials Integration. *Adv. Funct. Mater.* **2021**, *31*, No. 2008818.
(54) Kruth, J.-P.; Mercelis, P.; Van Vaerenbergh, J.; Froyen, L.; Rombouts, M. Binding Mechanisms in Selective Laser Sintering and Selective Laser Melting. *Rapid Prototyping J.* **2005**, *11* (1), 26−36.
(55) Dorozhkin, S. V. Amorphous Calcium (ortho)phosphates. *Acta Biomater.* **2010**, *6* (12), 4457−4475.
(56) Bannerman, A.; Williams, R. L.; Cox, S. C.; Grover, L. M. Visualising Phase Change in a Brushite-Based Calcium Phosphate Ceramic. *Sci. Rep.* **2016**, *6*, No. 32671.
(57) Uskoković, V.; Marković, S.; Veselinović, L.; Škapin, S.; Ignjatović, N.; Uskoković, D. P. Insights into the Kinetics of Thermally Induced Crystallization of Amorphous Calcium Phosphate. *Phys. Chem. Chem. Phys.* **2018**, *20* (46), 29221−29235.
(58) Stammeier, J. A.; Purgstaller, B.; Hippler, D.; Mavromatis, V.; Dietzel, M. Raman Spectroscopy of Amorphous Calcium Phosphate to Crystalline Hydroxyapatite Transformation. *MethodsX* **2018**, *5*, 1241−1250.
(59) Tachibana, A.; Kaneko, S.; Tanabe, T.; Yamauchi, K. Rapid Fabrication of Keratin-Hydroxyapatite Hybrid Sponges toward Osteoblast Cultivation and Differentiation. *Biomaterials* **2005**, *26* (3), 297−302.
(60) Hirata, I.; Akamatsu, M.; Fujii, E.; Poolthong, S.; Okazaki, M. Chemical Analyses of Hydroxyapatite Formation on SAM Surfaces Modified with COOH, NH(2), CH(3), and OH Functions. *Dent. Mater. J.* **2010**, *29* (4), 438−445.
(61) Sengupta, I.; Bhattacharya, P.; Talukdar, M.; Neogi, S.; Pal, S. K.; Chakraborty, S. Bactericidal Effect of Graphene Oxide and Reduced Graphene Oxide: Influence of Shape of Bacteria. *Colloids Interface Sci. Commun.* **2019**, *28*, 60−68.
(62) Stich, T.; Alagboso, F.; Křenek, T.; Kovářík, T.; Alt, V.; Docheva, D. Implant-Bone-Interface: Reviewing the Impact of Titanium Surface Modifications on Osteogenic Processes in Vitro and in Vivo. *Bioeng. Transl. Med.* **2022**, *7* (1), No. e10239.
(63) Zambrano, B. L.; Renz, A. F.; Ruff, T.; Lienemann, S.; Tybrandt, K.; Vörös, J.; Lee, J. Soft Electronics Based on Stretchable and Conductive Nanocomposites for Biomedical Applications. *Adv. Healthcare Mater.* **2021**, *10* (3), No. 2001397.
(64) Ghiasi, M. S.; Chen, J.; Vaziri, A.; Rodriguez, E. K.; Nazarian, A. Bone Fracture Healing in Mechanobiological Modeling: A Review of Principles and Methods. *Bone Rep.* **2017**, *6*, 87−100.
(65) Khaw, J. S.; Xue, R.; Cassidy, N. J.; Cartmell, S. H. Electrical Stimulation of Titanium to Promote Stem Cell Orientation, Elongation and Osteogenesis. *Acta Biomater.* **2022**, *139*, 204−217.
(66) Staehlke, S.; Bielfeldt, M.; Zimmermann, J.; Gruening, M.; Barke, I.; Freitag, T.; Speller, S.; Van Rienen, U.; Nebe, B. Pulsed Electrical Stimulation Affects Osteoblast Adhesion and Calcium Ion Signaling. *Cells* **2022**, *11* (17), No. 2650.
(67) Li, L.; Zhang, X.; Zhou, J.; Zhang, L.; Xue, J.; Tao, W. Non-Invasive Thermal Therapy for Tissue Engineering and Regenerative Medicine. *Small* **2022**, *18* (36), No. 2107705.
(68) Luong, D. X.; Yang, K.; Yoon, J.; Singh, S. P.; Wang, T.; Arnusch, C. J.; Tour, J. M. Laser-Induced Graphene Composites as Multifunctional Surfaces. *ACS Nano* **2019**, *13* (2), 2579−2586.
(69) Lipovka, A.; Fatkullin, M.; Shchadenko, S.; Petrov, I.; Chernova, A.; Plotnikov, E.; Menzelintsev, V.; Li, S.; Qiu, L.; Cheng, C.; Rodriguez, R. D.; Sheremet, E. Textile Electronics with Laser-Induced Graphene/Polymer Hybrid Fibers. *ACS Appl. Mater. Interfaces* **2023**, *15*, 38946.

https://doi.org/10.1021/acsami.4c21046
ACS Appl. Mater. Interfaces XXXX, XXX, XXX−XXX